Tracking eddies in a regional model of the "Cape Basin" off South Africa.

A. M. Doglioli
Laboratoire de Physique des Océans, UMR 6523 CNRS/IFREMER/UBO, Brest, France

B. Blanke
Laboratoire de Physique des Océans, UMR 6523 CNRS/IFREMER/UBO, Brest, France

S. Speich
Laboratoire de Physique des Océans, UMR 6523 CNRS/IFREMER/UBO, Brest, France

G. Lapeyre
Laboratoire de Météorologie Dynamique, École Normale Supérieure/IPSL, Paris, France

A. M. Doglioli, LPO, Laboratoire de Physique des Océans, UMR 6523 CNRS/IFREMER/UBO, UFR Sciences et Techniques, 6 avenue Le Gorgeu - C.S. 93837, 29238 Brest Cedex 3, France. (Andrea.Doglioli@univ-brest.fr)

Abstract.

The main goal of our study is to propose objective and quantitative tools to better evaluate the net mass exchanges across the "Cape Basin Cauldron" between the Southern Ocean, the South Atlantic and the Indian Basin. Our work is done in a regional ocean model that accounts for eddy displacements within this region where mesoscale eddies are an important means of transporting and distributing temperature and salt. Our wavelet analysis identifies objectively three-dimensional coherent structures in a simulation with $\frac{1}{10}^{\circ}$resolution. Furthermore, it enables to track eddy trajectories and time evolution of eddy properties. Mass transports are calculated from the knowledge of instantaneous values of eddy volume, diameter and drift velocity. Numerical Lagrangian computations coupled with the wavelet-based definition of each eddy allow the diagnostic of the origins and fates of the water masses brought into play. Our preliminary results shed light on the dynamical and thermodynamical behavior of modeled cyclones and anticyclones. For both types of structures, we find waters originating in the South Atlantic and the Indian Ocean. We interpret the differences between cyclones and anticyclones mostly in terms of contrasts in the proportion of the two geographical origins and in remote water mass properties.

Keywords: Oceanic eddies, regional modeling, Agulhas Current system, Southeast Atlantic Ocean, wavelets, Lagrangian diagnostics.

1. Introduction

Ocean heat and salt fluxes around Southern Africa are thought to be a key link in maintaining the global thermohaline circulation [*Gordon*, 2003]. The Agulhas Current is indeed the most intense western boundary current of the World Ocean and its retroflection shows one of the highest signals in eddy kinetic energy. Intensive Eulerian and Lagrangian observations combined with satellite data contribute to the description of this rich and complex area [e.g., *Richardson and Garzoli*, 2003; *Boebel and Barron*, 2003; *van Aken et al.*, 2003]. Mesoscale eddies and large current rings pinch off from the Agulhas Retroflection. The former are thought to impact the dynamics and variability of the South Benguela upwelling system [*Blanke et al.*, 2002, 2005], which represents one of the World Ocean richest ecosystems and major fishing area. The latter allow an Indian water leakage to the Atlantic Ocean [*Gordon*, 2003; *Richardson et al.*, 2003]. Recently, *Boebel et al.* [2003] reviewed the theories proposed for the Indo-Atlantic inter-ocean exchange. They limited the concept of "isolated Agulhas Rings embedded in a sluggish Benguela Drift" to the northwestern Cape Basin. They called "Cape Cauldron" the southeastern Cape Basin, where mesoscale cyclone/anticyclone interactions result in vigorous stirring and mixing.

Satellite measurements make possible rough estimates of the transport achieved by the eddy field [*van Ballegooyen et al.*, 1994], but gaps in knowledge of the full three-dimensional (3D) identity of these structures obstruct more accurate diagnostics. *Treguier et al.* [2003] quantified Agulhas eddy fluxes in a $1/6^o$ model of the Atlantic Ocean. One of their methods break down the total fluxes into "background" and "trapped eddy fluxes".

They defined and followed eddies with a criterion based on sea-surface height anomalies. They estimated volumes from heat and salt anomalies, assuming that eddies are sufficiently nonlinear so that anomalies are limited to the eddy core down to a trapping depth. From the volume of an average eddy and the approximate number of occurrences per year, *Treguier et al.* [2003] obtained an annual mean trapped eddy flux of warm water of 2 Sv.

Our work focuses on the analysis of a regional ocean model and aims at identifying mesoscale eddies with objective methods, tracking these eddies in time and evaluating the properties and the volume of water they transfer. Our identification is based on the wavelet analysis of model dynamic fields. Indeed, wavelets form an efficient basis set for localized structures such as ocean eddies. The main advantage of wavelets is to provide information about a function or dataset with respect to scale and location in contrast to Fourier transforms, which provide a one-parameter family of coefficients representing the global frequency content. *Jameson and Miyama* [2000] applied wavelet analysis to the numerical resolution of Kelvin and Rossby waves. *Luo and Jameson* [2002] presented an application of wavelet analysis to time-evolving structures such as eddies and fronts described by numerical modeling or by satellite data. In particular, they processed TOPEX/Poseidon satellite data, and successfully identified eddies in two-dimensional images.

In this paper, we focus mostly on two eddies, one anticyclone and one cyclone, that we obtained in a numerical simulation of the ocean dynamics around Southern Africa. The ocean model is presented in section 2. In section 3, we introduce a method to identify 3D coherent structures and to follow them in time. In section 4, we apply this method

to both eddies and we diagnose remote origins for the water masses they transfer. Then conclusions are drawn in section 5.

2. Ocean model

Our numerical configuration has been developed for the study of the Cape Basin and is based on the UCLA-IRD version of the Regional Ocean Modeling System (ROMS). The reader is referred to *Shchepetkin and McWilliams* [2003, 2005] for a more complete description of the numerical code. The model domain extends from 5.8°E to 34°E and from 25.4°S to 44°S (Fig. 1). The model grid is 283 × 229 points with a resolution of $\frac{1}{10}^\circ$ which corresponds to a mean grid spacing of 9 km, that samples correctly the first baroclinic Rossby radius of deformation throughout the whole area (about 30 km according to *Chelton et al.* [1998]). The grid is isotropic and does not introduce any asymmetry in the horizontal dissipation of turbulence. Therefore, it allows a fair representation of mesoscale dynamics. The bottom topography is derived from a 2' resolution database [*Smith and Sandwell*, 1997]. Although a numerical scheme associated with a specific equation of state limits errors in the computation of the horizontal pressure gradient [*Shchepetkin and McWilliams*, 2003], the bathymetry has been filtered in order to keep a slope parameter smaller than 0.3 [*Beckmann and Haidvogel*, 1993]. To preserve a sufficient resolution in the upper ocean, the model has 32 vertical levels. The vertical s-coordinate is stretched [see *Haidvogel and Beckmann*, 1999] to obtain a vertical resolution ranging from a minimum of 30 cm to a maximum of 6.25 m for the surface layer and from 31 cm to 1086 m for the bottom layer. All the model external forcing functions are derived from climatologies. At the surface, the model heat and fresh water fluxes are extracted from the Comprehensive Ocean-Atmosphere Data Set (COADS) ocean surface monthly

climatology [*Da Silva et al.*, 1994]. For the wind stress, a monthly mean climatology is computed from QuikSCAT satellite scatterometer data gridded at a $\frac{1}{2}^{\circ}$ resolution [*Liu et al.*, 1998]. At the four lateral boundaries facing the open ocean, an active, implicit, upstream-biased, radiation condition connects the model solution to the surroundings [*Marchesiello et al.*, 2001]. In the case of inflow conditions, the solution at the boundary is nudged toward seasonal, time-averaged outputs of the OCCAM global ocean model run at a $\frac{1}{4}^{\circ}$ resolution [*Saunders et al.*, 1999]. The model solution is started from rest and is calculated for 8 years. It reaches a statistical equilibrium after a spin-up of about 3 years. Model outputs are averaged and stored every 2 days of simulation.

3. Eddy identification and tracking

From the Wavelab library [http://www-stat.stanford.edu/~wavelab/] we developed a set of routines to analyze the circulation calculated by the ocean model. Our procedure can be decomposed into three steps: wavelet analysis, vertical tracking and time tracking.

3.1. Wavelet Analysis

Wavelet analysis provides methods for efficient data compression of variety of signals such as images or sounds. Here we use wave packets to decompose successive horizontal maps of relative vorticity and to extract localized structures in space. The wavelet analysis consists in the decomposition of the signal into orthogonal, multiresolution wave packets, in a manner similar to Fourier decomposition. A wave packet is a square integrable modulated waveform well localized in both position and frequency. We choose the Haar basis that is an orthonormal basis of $L^2(R^2)$ [*Daubechies*, 1988, 1992]. The algorithm we use has four different sub-steps: first, a best basis is found to minimize a cost function

(here the Shannon entropy) [*Wickerhauser*, 1994; *Coifman and Wickerhauser*, 1992]. This basis varies according to each time step considered and allows to find the best location for the wave packets. Second, the model relative vorticity is decomposed on this basis. Third, the wavelets are sorted as a function of their spectral coefficients. Only a few of them are kept with a number that depends on the dimension of the basis (usually 9% of the initial set of wavelets) and the other ones are set to zero. The method acts as pattern recognition since the reconstructed signal is zero where there is no identified pattern. Four, we extract structures so that adjacent points along x and y axes belong to the same pattern. Following this method, we obtain localized structures in space, which allows us to define and separate eddies.

We performed several tests to identify and optimize the parameters involved in this first step of the analysis. Applying the wavelet filtering to relative vorticity gives the best results both in terms of computing time and eddy identification. Other fields, such as the Okubo-Weiss criterion [*Okubo*, 1970; *Weiss*, 1991] or potential vorticity give similar results in eddy identification but require more calculations. It turns out that the critical parameter of the wavelet analysis is the minimal area set for the acceptance of an eddy. We set it to 1500 km^2 (i.e., a 22 km diameter in case of a circular shape) in order to reduce noise and superposition of multiple structures. We also defined a cut-off threshold at 0.2×10^{-5} [s^{-1}] when preprocessing relative vorticity.

At the end of this step, each structure is numbered and its area A is measured. The eddy center is defined with a precision corresponding to the model grid spacing as the gridpoint of local

$$\max_A(|\zeta|) \text{ or } \min_A(|u^2 + v^2|)$$

where ζ is the relative vorticity and u and v are the zonal and meridian velocity components, respectively. The criterion is chosen to allow the longest possible tracking. For the moment, we define the diameter D as the maximum between the zonal (D^{EW}) and the meridional (D^{NS}) arc lengths that intercept each eddy center with both endpoints on the edge of the structure. This definition takes into account the fact that the shape of eddies in the study area is frequently stretched and it will be useful in the instantaneous transport definition (see Appendix A and section 4.1).

Fig. 2 shows the 128×128 gridpoint domain used for the wavelet analysis. The domain spans the Benguela upwelling area to the north of the Agulhas retroflection. The relative vorticity map is calculated at -200 m at the same instant as Fig. 1, i.e., in summer during the last year of simulation. We could identify 12 patterns: some structures are superimposed; a few others are not eddies but rather filaments or meanders. On the other hand, structures such as #9 and #11 are well defined cyclonic and anticyclonic eddies, respectively. Their signal is also clearly present in the surface height field (Fig. 1). Cyclone #9 and anticyclone #11 are hereafter referred to as Asterix and Panoramix, respectively.

The wavelet analysis is able to detect most eddies, but not all of them. The reason is that some eddies have a velocity signature at -200 m but no vorticity signature. We prefer to analyze vorticity because it gives an objective criterion to detect eddies: a quasi-circular shape of the velocity field could be even more easily associated with large-scale meanders. Some large-scale structures resembling to meanders (such as structure 3 in Fig. 2) are already detected and may be associated with interaction between small-scale vortices.

3.2. Vertical tracking

The above analysis is repeated to diagnose the vertical extent of an eddy identified at -200 m. We chose this depth to start the analysis to eliminate the model superficial layers that are likely to account for a dynamics too much sensitive to air-sea interactions. We state that a structure identified at level z belongs to an eddy already identified at level $z - \Delta z$, when the criterion

$$c_z \in \mathfrak{E}_{z-\Delta z} \tag{1}$$

is satisfied, where $c_z \equiv (ic, jc)_z$ is the center of the structure identified at level z and $\mathfrak{E}_{z-\Delta z}$ is the set of gridpoints of the selected eddy at level $z - \Delta z$. After sensitivity tests and time computing considerations, we set the distance between two successive horizontal slices to $\Delta z = 100$ m.

The definition of the lower limit is somewhat more complex as our identification of coherent structures in the vertical direction is based purely on vorticity and may not account for the coherence of other fundamental properties as tracer anomalies. Therefore, we calculated a reference state for the model for all prognostic variables, averaging dynamic and thermodynamic fields over the last five years of simulation. For each archived model time step, we calculated potential density anomalies as [*Carton*, 2001]:

$$\delta\Pi = (f + \zeta)\frac{\partial_z \rho}{\rho} - f_o \frac{\partial_z \rho_o}{\rho_o}, \tag{2}$$

where f is the Coriolis parameter and ρ is the potential density calculated with a non-linear equation of state for seawater [*Jackett and McDougall*, 1995]. Subscript o refers to the model reference state. Tracer anomalies indicate properly the presence of both eddies in the upper 1000-1500 m (Fig. 3 and Fig. 4). Cyclones show $\Delta T < 0$, $\Delta S < 0$, whereas

anticyclones show $\Delta T > 0$, $\Delta S > 0$. Temperature plays a crucial role in determining the sign of density anomalies (positive for cyclones, negative for anticyclones) and salinity behaves much more like a passive tracer. Unlike tracers, velocity and potential vorticity anomaly profiles show a "top to bottom" extent for eddies. Indeed, the simulation we analyze is too short to reproduce properly the deep ocean dynamics. In this case, an eddy that develops in the upper 1000-1500 m tends to be barotropic (or equivalent-barotropic in the quasi-geostrophic approximation) and induces a slow rotation in the lower layer because of potential vorticity conservation. Furthermore, the OCCAM climatology used at the open boundaries may not represent very well the real stratification observed in the area.

All things considered, the depth at which salinity anomalies change sign is seen as a robust index to identify the deepest extension (z_L) acceptable for each selected eddy. Our procedure automatically recognizes this value (upper middle panels in Fig. 3 and Fig. 4) and the wavelet analysis of each horizontal slice of relative vorticity is repeated on the vertical to reach at least depth z_L. In this way, at a fixed time step, the area A_k and diameter D_k are diagnosed at each level k and the volume taken up by each eddy can be calculated as

$$V = \sum_k A_k \cdot \Delta z.$$

3.3. Time tracking

In order to track identified eddies with time, the criterion

$$c_{t,z=-200} \in \mathfrak{E}_{t-\Delta t,z=-200} \tag{3}$$

must be satisfied, where $c_{t,z=-200} \equiv (ic, jc)_{t,z=-200}$ is the eddy center at time t and depth -200 m and $\mathfrak{E}_{t-\Delta t}$ is the set of gridpoints of the same eddy at the previous time step. Several tests showed that the model output period, $\Delta t = 2$ days, does not bias the analysis. Though time tracking in backward and forward directions represents virtually equivalent techniques when using criterion (3), the backward direction has the advantage of an easier initialization. Indeed, well formed eddies are more easily found away from their formation region, in the westernmost part of the domain, and then tracked backward all the way to their ejection. Fig. 5 shows the 3D envelope of both eddies calculated month after month. The trajectories of the eddy centers at -200 m are shown in projection on the ocean bottom every 2 days.

At each time step we store the instantaneous velocity v, the volume V and the diameter D of each coherent eddy. The velocity is calculated as the distance covered by the eddy center over successive 2-day time intervals. The knowledge of these three quantities will enable the calculation of the instantaneous transport Tr of each coherent eddy (see Appendix A and section 4.1).

3.4. Lagrangian particles

The ARIANE toolkit is an off-line Lagrangian diagnostic tool dedicated to the analysis of simulations run with numerical ocean models [*Blanke and Raynaud*, 1997, http://fraise.univ-brest.fr/lpo/ariane/]. The analytical calculation of 3D streamlines, for periods over which the velocity field is assumed to be constant, defines a convenient way to derive particle trajectories within any model gridcell, before reconstruction over the full model mesh scale. In our framework, Lagrangian particles are disseminated within the 3D volume of the two eddies we selected with the wavelet analysis. On each vertical level between

$z = -200$ m to $z = z_L$ separated by $\Delta z = 50$ m, we uniformly distribute 4 particles among each horizontal gridcell. We perform two types of experiments. First, in order to study coherent eddy properties, particles are disseminated within the eddy at the end of its lifetime and Lagrangian trajectories are integrated backward in time till the eddy formation is reached. In this case, properties such as tracer values are interpolated over each trajectory and stored at the nominal sampling period of the model output (2 days). Second, in order to study remote water mass origins, particles are disseminated within the eddy at different instants of its lifetime and integrated backward for a time (3 years) much longer than the coherent eddy lifetime. Then, the trajectories are stopped when the particles are intercepted by the model open boundaries. The emphasis is put here on geographical origins, with the definition of 6 regions of interception: North (representing the Benguela Current region), Northwest and Southwest (South Atlantic Gyre), South (South Atlantic Current), Southeast (Agulhas Return Current) and Northeast (Agulhas Current).

4. Results and discussion

A high level of mesoscale activity develops during the 8-year simulation, with the generation of Agulhas rings and the shedding of cyclonic eddies from the southern tip of the Agulhas Bank and from the Benguela slope. Off the west coast, the upwelling front shows an important variability, developing meanders, plumes and filaments in a realistic manner. The model reproduces shear-edge cyclonic eddies in the bight of Agulhas Bank in good agreement with observed features [e.g. *Lutjeharms et al.*, 1989, 2003] in particular for their vertical and horizontal scales. We analyzed the average behavior of the model

solution and its variability. We found a fair agreement between simulated and observed circulation patterns, both at the surface and at deeper levels.

4.1. Coherent eddies

In slightly more than five months (day 1 / month 10 / year 7 to 6/2/8, in southern spring and summer) Asterix moves west-southwestward (Fig. 5a). Anticyclone Panoramix is tracked for slightly less than 4 months from 5/7/7 to 15/10/7 (in southern winter and spring) and moves to the northwest (Fig. 5b). This divergence in eddy pathways has been observed in satellite and drifter data [*Boebel et al.*, 2003; *Morrow et al.*, 2004]. According to *Morrow et al.* [2004], it is induced by changes in planetary and relative vorticity at the eddy flanks.

The time series of Asterix drift velocity (Fig. 6a top) shows accelerations and decelerations corresponding to cusp points in the trajectory. The calculation of the associated error bars is detailed in Appendix A. The volume and diameter (Fig. 6a middle and bottom) show significant variability at the stage of eddy formation, when the structure pinches off from the mean current. Then, there is a central period during which the eddy is well structured and its volume and diameter do not vary much as it moves in the Cape Basin. The variations in volume and diameter are small and demonstrate that our algorithm for eddy identification works well. Eddies that do not interact with their surroundings would conserve exactly their properties with time. The decrease in volume and diameter of Panoramix (Fig. 6b middle and bottom) between 20 and 50 days of its lifetime may be due to the interaction with the western open boundary when the anticyclone goes around to the Vema seamount (Fig. 5b). Similarly, during the final 10 days, both the cyclone and the anticyclone are close to the western open boundary, where the

ocean model is less successful at depicting coherent mesoscale structures. For both eddies, large standard deviations in diameter that do not correspond to large standard deviations in volume are the sign of stretched shapes.

Time series of instantaneous eddy transport with error bars are reported in Fig. 7. Modulations in time are mainly driven by changes in velocity. Asterix transport is always larger than Panoramix. For Asterix, the error is equally distributed on the three variables used to derive the transport, while for Panoramix the error is mainly due to the poor estimation of the volume during the central period. Time mean velocity, diameter, volume and transport for Asterix are $\overline{v} = 0.08$ ms^{-1}, $\overline{D} = 179$ km, $\overline{V} = 15.8 \cdot 10^{12}$ m^3 and $\overline{Tr} = 0.69$ Sv, respectively. Equivalent quantities for Panoramix are 0.11 ms^{-1}, 147 km, $5.9 \cdot 10^{12}$ m^3 and 0.41 Sv.

A first comparison with data from the KAPEX experiment [*Boebel et al.*, 2003] shows that model eddy diameters are similar to those observed (for cyclones and anticyclones). Observations reported by *Boebel et al.* [2003] and *Morrow et al.* [2004] show also that anticyclones move faster than cyclones, but that eddy drift velocities diagnosed in our model are too large (by roughly a factor of 2). Instead, cyclonic and anticyclonic eddies tracked by *van Ballegooyen et al.* [1994] have drift velocity between 0.04 ms^{-1} and 0.09 ms^{-1}, in closer correspondence with our estimates. The difference between model data and observations can be partly explained by the shortness of our tracking. The domain size does not allow us to follow eddies during their whole lifetime and our velocity estimates are done during the very first months when the structures are the most energetic and move more rapidly than afterwards. Nevertheless, we note that the volumes for anticyclones

estimated by *van Ballegooyen et al.* [1994] are comparable with the volume obtained for Panoramix.

For the first type of Lagrangian experiment, we inseminated the cyclone and the anticyclone with 9920 and 5472 particles, respectively. Initialization is performed close to the western open boundary and Lagrangian trajectories are integrated backward in time. The trajectories show that the particles are trapped within each eddy and follow closely the trajectory diagnosed with the wavelet analysis (Fig. 8). This is a robust validation of the ability of the wavelet analysis to track eddy cores with time. The particles inseminated in the deepest layer of Panoramix are found to leave the core of the eddy before the end of the backward time integration (Fig. 8b). The explanation is likely again an interaction with the western open boundary at the time the anticyclone turns around the Vema seamount.

Tracer conservation is not found at the scale of individual model levels within each eddy, which suggests the existence of mixing processes. Fig. 9 shows the time series for temperature and salinity averaged over the area of the eddy considered at -200 m (Eulerian calculation). We computed density (in sigma zero units) from local values of temperature and salinity via non-linear equation of state by *Jackett and McDougall* [1995]. Standard deviations are larger for the cyclone (Fig. 9a) than for the anticyclone, mainly because of the larger area of the cyclone. A strong correlation is observed between temperature and salinity trends. This is especially true for the cyclone (Fig. 9a) that shows a progressive gain of buoyancy with warming and salinization occurring simultaneously. On the other hand, the anticyclone (Fig. 9b) shows progressive cooling and densification at -200 m. Similar trends are obtained with Lagrangian calculations based on particles displacements

(not shown here). This suggests a possible mixing of the eddy waters with surrounding waters or a signature of the atmospheric forcing. Spiciness [*Schmitt*, 1999] and overturning circulation within the surface mixed layer [*Donners et al.*, 2004] might also be in play.

4.2. Remote origins

The second type of Lagrangian experiments is summarized in Table 1. Two initializations were done at different instants of both eddy lifetimes (two months and one month apart for cyclone Asterix and anticyclone Panoramix, respectively). The number of particles in use slightly varies due to small differences in eddy volumes at different times (see also Fig. 6). Then trajectories were integrated backward in time for a maximum of 3 years. Before the end of this integration and for both eddies, a very large number of particles are intercepted by either of the 6 control sections in use.

For cyclone Asterix (first and second columns) we obtain very similar results for the two initializations. About half of the particles come from the Agulhas Current (NEast) and 37% originate in the Atlantic (SWest+NWest). The percentage of the particles flowing from the Benguela Current (North), the South Atlantic (South) and the Agulhas Return Current (SWest) is small. For anticyclone Panoramix (third and forth columns) the percentages depend on the initialization. The major difference is the increase of the Benguela origin (North) at the expense of the Agulhas origin, probably because of mixing with surrounding water masses during the northwestward movement of the eddy. Furthermore, as discussed above, the uncertainty on the volume calculation for the anticyclone is larger than for the cyclone. However, the percentage of the particles that come from the Agulhas Current is increased in comparison with the cyclone, whereas the percentage obtained for

the South Atlantic origin drops and the contribution from the subtropical Indian Ocean (SEast) and the Benguela region (North) increases.

The difference between the percentages of Agulhas and Atlantic waters partially explains the cold and fresh anomaly of the cyclone with respect to surrounding waters, as well as the warm and salty signal carried by the anticyclone. As a high percentage of Agulhas origin is also found for cyclone Asterix this first explanation cannot however account for all the difference. Following the technique introduced by *Blanke et al.* [1999], the passage of each particle, with the volume it represents, is recorded and summed on each velocity point of the model three-dimensional grid. We limit the calculation to the particles intercepted by the remote control sections. The subsequent three-dimensional nondivergent pseudo transport field can be projected along the vertical direction, and pictured as a streamfunction. Isolines correspond to the general features of the movement, though they do not necessarily match any individual trajectory, and the spacing between them characterizes the spreading along the movement (Fig. 10). For both Asterix and Panoramix, the Agulhas inflow is strong, but particles from the cyclone flow closer to the coast than those from the anticyclone. The Cape Cauldron area is the crossroads for particles coming from the Agulhas Current and particles coming from sections South and North, for Asterix and Panoramix, respectively (see Table 1). Furthermore, the particles from the anticyclone are the fastest to connect the Agulhas Current to the western domain (361 vs. 427 days, for experiments P46 and A33, respectively). This makes property conservation easier.

Another element of explanation is found in specific water mass properties for each origin. Fig. 11 shows the distribution of the particles within the Agulhas Current over the

NEast interception section. The comparison of the results of experiments A33 and P46 shows that the particles associated with the cyclone (Fig. 11a) are deeper (mean depth $< z >= 670$ m) than the particles associated with the anticyclone ($< z >= 478$ m). They are thus colder ($< T >= 10.2^o$C vs. $< T >= 13.2^o$C) and fresher ($< S >= 34.85$ psu vs. $< S >= 35.01$ psu). An equivalent behavior is found for the South Atlantic origin: mean properties are $< z >= 710$ m, $< T >= 7.7^o$C, $< S >= 34.65$ psu for the cyclone, and $< z >= 389$ m, $< T >= 12.0^o$C, $< S >= 34.89$ psu for the anticyclone.

5. Summary and conclusions

Interocean mass and property exchanges are thought to play an important role in the evolution of present-day global climate, particularly in response to variations of heat and freshwater fluxes along the thermohaline circulation. In this respect, the oceanic region around Southern Africa is a critical water mass crossroads within the so-called warm-water route of the global overturning circulation [*Gordon*, 1986; *Gordon et al.*, 1992; *Gordon*, 2003]. Oceanic eddies are important in distributing properties like heat and salt throughout the World's Oceans, and Agulhas rings are thought to play a key role in the Indo-Atlantic interocean exchange [*Gordon*, 1986; *de Ruijter et al.*, 1999; *Weijer et al.*, 1999]. Nevertheless, while this Indo-Atlantic connection appears crucial in global ocean models [*Speich et al.*, 2001, 2002], recent studies based on observations challenge this hypothesis because of the highly nonlinear regime found in the Cape Basin (the first Atlantic basin to collect leakage of Agulhas water). Turbulence is so intense in the area that it could prevent the continuous advection of Indian or South Atlantic waters [*de Ruijter et al.*, 1999; *Boebel et al.*, 2003]. Indeed, in the Cape Basin, eddies of different types interact with each other and with the main retroflection of the Agulhas Current,

in a context of vigorous stirring and mixing [*Gordon*, 2003; *Boebel et al.*, 2003; *Morrow et al.*, 2004].

In this turbulent framework and in order to better evaluate the net mass exchanges across this complex region, the main goal of our study was to propose objective and quantitative diagnostic tools to estimate the proportion of Agulhas leakage that contributes to the upper branch of the global overturning circulation. This work is done in a regional ocean model that accounts for eddy displacements within the Cape Basin region.

The approach we developed is able to objectively identify 3D coherent structures in a simulation with a $\frac{1}{10^o}$ horizontal resolution. It can track eddy trajectories as well as the evolution of their properties. Because we needed first to validate the method, we studied only a few of the numerous mesoscale structures simulated by the model. We decided to focus on two different types of mesoscale vortices. The first type is made of cyclonic eddies ejected into the open ocean from the Southwestern African continental slope. The second type is made of warm anticyclonic Agulhas rings that are characterized by Indian Ocean thermocline water properties. Our tracking shows divergent pathways for both types. The anticyclone propagates westward and equatorward with a typical speed of 0.11 ms^{-1} whereas the cyclone propagates westward and poleward at 0.08 ms^{-1}. This behavior is very similar to that observed with altimetry along different subtropical eastern boundaries [*Morrow et al.*, 2004]. Our values are however slightly larger than those derived from altimetry and RAFOS floats, but with the use of different tracking criteria [*van Ballegooyen et al.*, 1994; *Boebel et al.*, 2003; *Morrow et al.*, 2004].

The wavelet analysis allows us to follow eddies in space and time as long as they exist as coherent structures. As we are able to define the envelope of each eddy, we can seed its

entire volume with Lagrangian particles and calculate their 3D trajectories, backward or forward in time, in the modeled velocity field. This is used to track either the origins of the water masses that explain the thermodynamical structure of an eddy or the fate of the waters that it encompasses: water properties can be tracked before the eddy formation and after its consumption. We applied such Lagrangian calculations to both eddy types. In the simulation we analyze, the anticyclone and the cyclone drag the most important fraction of their volume from the Agulhas Current system in the Indian Ocean. This result is supported by recent work on hydrology applied to the characterization of Cape Basin eddies [*Giulivi and Gordon*, 2005]. In our model, the characteristics of cyclones and anticyclones are different, the cyclone being fresher and colder than the anticyclone. This is due in part to their different constitution in Agulhas water itself, as the cyclone draws water from deeper layers. Secondly, the cyclone is also fed significantly with fresh and relatively cold waters from the South Atlantic. Finally, the advective time scales from these remote regions to the eddy generation location are longer for the cyclone than for the anticyclone, making the mixing of Agulhas and South Atlantic waters more efficient in the case of the cyclone.

Our Lagrangian computations coupled with the wavelet-based definition of each eddy volume allow the estimate of the mass transport achieved by each structure. This result represents a major achievement in itself because it makes possible, in models, the evaluation of the relevance of the ocean off South Africa to the return branch of the global thermohaline circulation. Heat and fresh water transport estimates will also be derived in a near future for each eddy type. Despite the robustness of our results with respect to the different methodologies we used to define, identify and track eddies, we have noted a

number of caveats before a thorough comparison with observed structures can be done. Our model domain is rather narrow in longitude and does not permit a full tracking of eddies during their whole lifetime: they interact too soon with the model open boundaries and sponge layers. Then, because of drift problems [*Donners and Drijfhout*, 2004], the OCCAM model that provides the large-scale thermohaline structure for the initial state and the open boundaries does not represent perfectly the temperature and salinity distribution in the first 1500 m of the ocean and is likely to bias the thermodynamical properties of the eddies we analyze. Our study focuses here on the development of tools adapted to the tracking of eddies in ocean models and develops appropriate diagnostics to characterize their properties. A more complete study is needed for an accurate evaluation of the net exchange of properties across the Cape Basin and of the complex role of mesoscale processes that can affect water mass origins and fates.

Acknowledgments. The authors wish to thank Michel Arhan and Xavier Carton for enlightening discussions about eddy dynamics. A. M. Doglioli is supported by SHOM, under contract number CA 2003/03/CMO (Contact: Alain Serpette). This study is also a contribution to InterUp, a project funded by the French Programme national Atmosphère et Océan à Multi-échelles (PATOM).

Appendix A: Transport definitions

We define the mass transport of a coherent eddy as the ratio between the eddy volume V and the time Δt needed to cross entirely a fixed section perpendicular to the direction of propagation of the eddy center:

$$Tr = V \cdot \Delta t^{-1}. \tag{A1}$$

Assuming that the time interval is $\Delta t = \Delta x \cdot v^{-1}$, where $\Delta x = D$ is the eddy diameter and v is the velocity of the eddy center, the transport is estimated as

$$Tr = v \cdot V \cdot D^{-1}. \tag{A2}$$

In our calculations, $v \equiv v(t) =< v(t,z) >$ is the vertical average of the velocity of the eddy center, as computed for each z-layer with a time-centered scheme involving successive positions. We estimate the relative error $v_{err} \equiv v_{err}(t)$ made on velocity as

$$v_{err} = \frac{\sigma_z(u)}{v}, \tag{A3}$$

where σ_z is the standard deviation of the distribution along the vertical axis.

As described above, the wavelet analysis provides the eddy volume at each time step. Our estimate of the relative error $V_{err} \equiv V_{err}(t)$ on the volume calculation is

$$V_{err}(t) = \frac{(z_L - iz_L) \cdot A_L}{V} + \frac{4\Delta x \Delta z \sum_{k=1}^{iz_L} A_k D_k^{-1}}{V}, \tag{A4}$$

that is the sum of errors due to the vertical (step Δz) and horizontal (step Δx) discrete representations of the eddy. The first term on the right-hand side is the volume of the cylinder that the method may neglect at the base of the eddy (depth z_L) because of a mismatch between z_L and the depth of the nearest discrete layer (iz_L) where the eddy area A_L is calculated. The second term is the approximate volume of a cylindrical ring neglected or taken by mistake around the eddy whose area A_k and diameter D_k are diagnosed at each level k.

We define diameter D as the maximum between the zonal (D^{EW}) and the meridional (D^{NS}) arc lengths that intercept each eddy center with both endpoints on the edge of the structure. Then, repeating this maximization at each level k, the reference diameter used

in A2 is

$$D = \max\left\{\max_z\{D_k^{EW}\}; \max_z\{D_k^{NS}\}\right\}. \quad \text{(A5)}$$

Definition A5 ensures that the full 3D structure of the eddy crosses the fixed section used to calculate its transport in A2.

A2 is exact for a circular eddy even if it is in rotation around its center. For stretched eddied in rotation, the relative error made on the calculation of D with A5 is estimated as

$$D_{err} = \frac{\left|\max_z\{D^{EW}\} - \max_z\{D^{NS}\}\right|}{D}. \quad \text{(A6)}$$

Finally, the relative error on our transport estimate is the sum of the errors defined in A3, A4 and A6:

$$Tr_{err} = v_{err} + V_{err} + D_{err}.$$

References

Beckmann, A., and D. Haidvogel (1993), Numerical simulation of flow around a tall isolated seamount. Part 1: Problem formulation and model accuracy, *J. Phys. Oceanogr.*, *23(8)*, 1736–1753.

Blanke, B., and S. Raynaud (1997), Kinematics of the Pacific Equatorial Undercurrent: An Eulerian and Lagrangian approach from GCM results, *J. Phys. Oceanogr.*, *27*, 1038–1053.

Blanke, B., M. Arhan, S. Speich, and G. Madec (1999), Warm water paths in the quatorial Atlantic as diagnosed with a general circulation model, *J. Phys. Oceanogr.*, *29*, 2753–2768.

Blanke, B., C. Roy, P. Penven, S. Speich, J. C. McWilliams, and G. Nelson (2002), Linking wind and upwelling interannual variability in a regional model of the southern Benguela, *Geophys. Res. Lett.*, *29*(24), 2188, doi:10.1029/2002GL015718.

Blanke, B., S. Speich, A. Bentamy, C. Roy, and B. Sow (2005), Modeling the structure and variability of the southern Benguela upwelling using QuikSCAT wind forcing, *J. Geophys. Res.*, *110*, C07018, doi:10.1029/2004JC002529.

Boebel, O., and C. Barron (2003), A comparison of in-situ float velocities with altimeter derived geostrophic velocities, *Deep-Sea Res. II*, *50*, 119–139.

Boebel, O., J. Lutjeharms, C. Schmid, W. Zenk, T. Rossby, and C. Barron (2003), The cape cauldron: a regime of turbulent inter-ocean exchange, *Deep-Sea Res. II*, *50*, 57–86.

Carton, X. (2001), Hydrodynamical modeling of oceanic vortices, *Surv. Geophys.*, *22*, 179–263.

Chelton, D. B., R. A. deSzoeke, M. G. Schlax, K. El Naggar, and N. Siwertz (1998), Geographical variability of the first-baroclinic Rossby radius of deformation, *J. Phys. Oceanogr.*, *28*, 433–460.

Coifman, R. R., and M. V. Wickerhauser (1992), Entropy based algorithms for best basis selection, *IEEE Trans. on Inf. Theory*, *32*, 712–718.

Da Silva, A. M. and Young, C. C. and Levitus,S. (1994), Atlas of surface marine data 1994, vol. 1, algorithms and procedures, *Tech. rep.*, U. S. Department of Commerce, NOAA.

Daubechies, I. (1988), Orthonormal basis of compactly supported wavelets, *Commun. Pure Appl. Math.*, pp. 909–996.

Daubechies, I. (1992), *Ten Lectures on Wavelets*, 357 pp., Society for Industrial and Applied Mathematics.

de Ruijter, W. P. M., A. Biastoch, S. S. Drijfhout, J. R. E. Lutjeharms, R. P. Matano, T. Pichevin, P. J. van Leeuwen, and W. Wijer (1999), Indian-Atlantic interocean exchange: Dynamics, estimation and impact, *J. Geophys. Res.*, *104*(C9), 20,885–20,910.

Donners, J., and S. S. Drijfhout (2004), The Lagrangian view of South Atlantic interocean exchange in a global ocean model compared with inverse model results, *J. Phys. Oceanogr.*, *34*, 1019–1035.

Donners, J., S. S. Drijfhout, and A. Coward (2004), Impact of cooling on the water mass exchange of Agulhas rings in a high resolution ocean model, *Geophys. Res. Lett.*, *31*, L16312, doi:10.1029/2004GL020644.

Giulivi, C. F., and A. L. Gordon (2005), Isopycnal displacements within the Cape Basin thermocline as revealed by the Hydrographic Data Archive, *Deep-Sea Res. I*, in press.

Gordon, A. L. (1986), Interocean exchange of thermocline water, *J. Geophys. Res.*, *91*, 5037–5046.

Gordon, A. L. (2003), The brawniest retroflection, *Nature*, *421*(6926), 904–905.

Gordon, A. L., R. F. Weiss, W. M. Smethie, and M. J. Warner (1992), Thermocline and Intermediate Water Communication between the South-Atlantic and Indian Oceans, *J. Geophys. Res.*, *97*, 7223–7240.

Haidvogel, D., and A. Beckmann (1999), *Numerical ocean circulation modeling*, vol. Series on environmental science and management Vol. 2, Imperial College Press.

Jackett, D. R., and T. J. McDougall (1995), Minimal adjustment of hydrographic profiles to achieve static stability, *J. Atmos. Ocean. Technol.*, *12*(4), 381–389.

Jameson, L., and T. Miyama (2000), Wavelet analysis and ocean modeling: A dynamically adaptive numerical method "WOFD-AHO", *Mon. Wea. Rev.*, *128*, 1536–1548.

Liu, W. T., W. Tang, and P. S. Polito (1998), NASA scatterometer provides global ocean-surface wind fields with more structures than numerical weather prediction, *Geophys. Res. Lett.*, *25*(6), 761–764.

Luo, J., and L. Jameson (2002), A wavelet-based technique for identifying, labeling, and tracking of ocean eddies, *J. Atmos. Ocean. Technol.*, *19*(3), 381–390.

Lutjeharms, J. R. E., R. Catzel, and H. R. Valentine (1989), Eddies and other border phenomena of the Agulhas Current, *Cont. Shelf Res.*, *9*, 597–616.

Lutjeharms, J. R. E., O. Boebel, and H. Rossby (2003), Agulhas cyclones, *Deep-Sea Res. II*, *50*, 13–34.

Marchesiello, P., M. J. C., and A. Shchepetkin (2001), Open boundary condition for long-term integration of regional oceanic models, *Ocean Model.*, *3*, 1–21.

Morrow, R., F. Birol, D. Griffin, and J. Sudre (2004), Divergent pathways of cyclonic and anti-cyclonic ocean eddies, *Geophys. Res. Lett.*, *31*, L24311, doi:10.1029/2004GL020974.

Okubo, A. (1970), Horizontal dispersion of floatable particles in the vicinity of velocity singularities such as convergences, *Deep-Sea Res.*, *17*, 445–454.

Richardson, P., and S. Garzoli (2003), Characteristics of intermediate water flow in the Benguela current as measured with RAFOS floats, *Deep-Sea Res. II*, *50*, 57–86.

Richardson, P. L., J. R. E. Lutjeharms, and O. Boebel (2003), Introduction to the "Inter-ocean exchange around southern Africa", *Deep-Sea Res. II*, *50*, 1–12.

Saunders, P. M., A. C. Coward, and B. A. de Cuevas (1999), Circulation of the Pacific Ocean seen in a global ocean model: Ocean Circulation and Climate Advanced Modelling project (OCCAM), *J. Geophys. Res.*, *104*(C8), 18,281–18,300.

Schmitt, R. W. (1999), Spice and the Demon, *Science*, *283*(5401), 498–499.

Shchepetkin, A. F., and J. C. McWilliams (2003), A method for computing horizontal pressure-gradient force in an oceanic model with nonaligned vertical coordinate, *J. Geophys. Res.*, *108*(C3), 3090, doi:10.1029/2001JC001047.

Shchepetkin, A. F., and J. C. McWilliams (2005), The regional oceanic modeling system (ROMS): a split-explicit, free-surface, topography-following-coordinate oceanic model, *Ocean Model.*, *9*, 347–304.

Smith, W. H. F., and D. T. Sandwell (1997), Global sea floor topography from satellite altimetry and ship depth soundings, *Science*, *227*, 1956–1962.

Speich, S., B. Blanke, and G. Madec (2001), Warm and cold water paths of a O.G.C.M. thermohaline conveyor belt, *Geophys. Res. Lett.*, *28*(2), 311–314.

Speich, S., B. Blanke, P. de Vries, S. Drijfhout, K. Döös, A. Ganachaud, and R. Marsh (2002), Tasman leakage: A new route in the global ocean conveyor belt, *Geophys. Res. Lett.*, *29*(10), 1416, doi:10.1029/2001GL014586.

Treguier, A., O. Boebel, B. Barnier, and G. Madec (2003), Agulhas eddy fluxes in a $1/6^o$ Atlantic model, *Deep-Sea Res. II*, *50*, 119–139.

van Aken, H. M., A. K. van Veldhoven, C. Vetha, W. P. M. de Ruijter, P. J. van Leeuwen, S. S. Drijfhout, C. P. Whittled, and M. Rouault (2003), Observations of a young Agulhas ring, Astrid, during MARE in March 2000, *Deep-Sea Res. II*, *50*, 167–195.

van Ballegooyen, R. C., M. L. Gründlingh, and J. R. E. Lutjeharms (1994), Eddy fluxes of heat and salt from the southwest indian Ocean into the southeast Atlantic Ocean: A case study, *J. Geophys. Res.*, *99*(C7), 14,053–14,070.

Weijer, W., W. P. M. de Ruijter, H. A. Dijkstra, and P. J. van Leeuwen (1999), Impact of interbasin exchange on the Atlantic overturning circulation, *J. Phys. Oceanogr.*, *29*, 2266–2284.

Weiss, J. (1991), The dynamics of enstrophy transfer in two-dimensional hydrodynamics, *Physica D*, *48*, 273–294.

Wickerhauser, M. V. (1994), *Adapted Wavelet Analysis from Theory to Software*, xii + 486 pp., AK Peters, Ltd., Wellesley, Massachusetts.

eddy	*ASTERIX*		*PANORAMIX*	
experiment	*A33*	*A45*	*P46*	*P47*
initialization	it6 M2 Y8	it6 M12Y7	it1 M10 Y7	it1 M9 Y7
particle number	9920	12224	5760	5728
intercepted %	96	96	98	99
lost %	4	4	2	1
NEast%	47	44	47	55
SEast%	3	3	6	6
South%	9	10	3	5
SWest%	29	30	15	18
NWest%	8	9	16	10
North%	1	1	11	5

Table 1. Remote geographical origins for both eddies. See text for explanations and Fig. 10 for the localization of the interception sections.

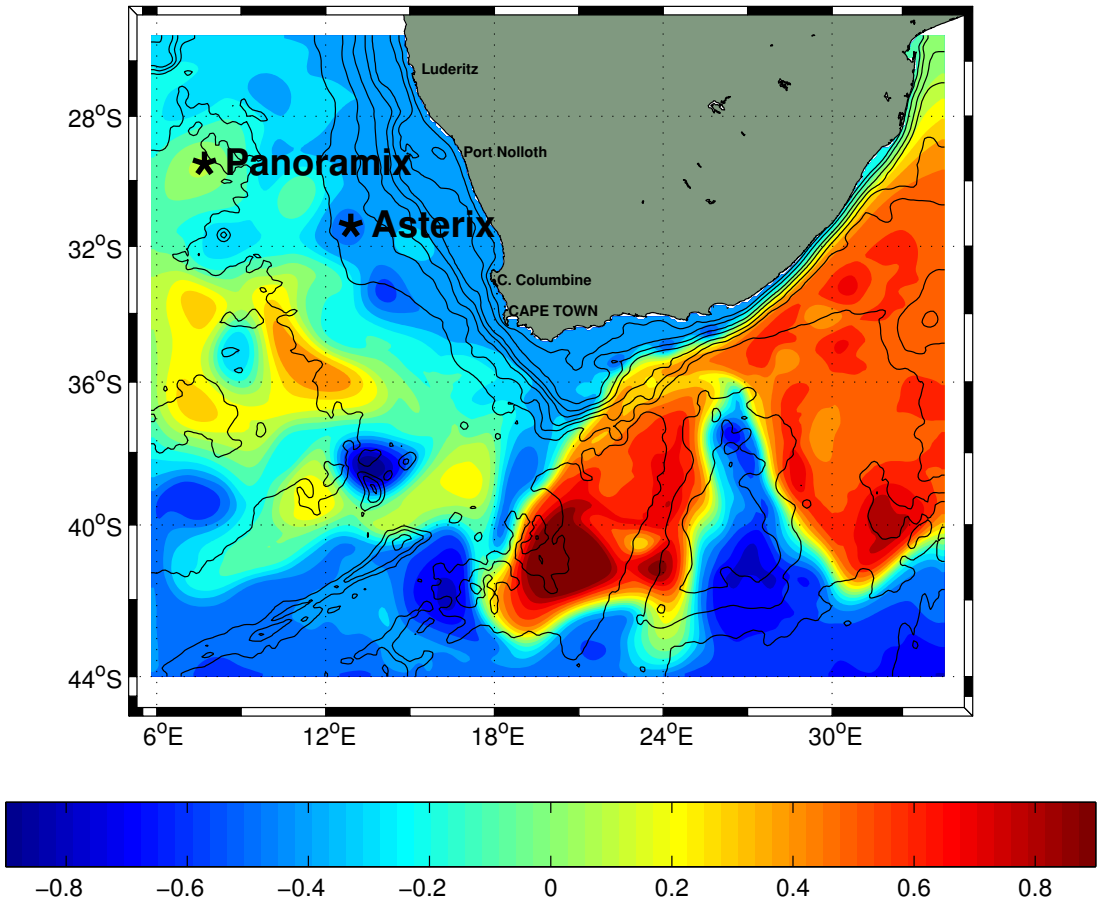

Figure 1. Model domain. Isobaths 100, 200, 500, 1000, 2000, 3000, 4000 and 5000 [m] are drawn in black. Shaded colors represent the surface height [m]. Positions on day 9 / month 10 / year 7 of anticyclone Panoramix and cyclone Asterix are indicated with a star.

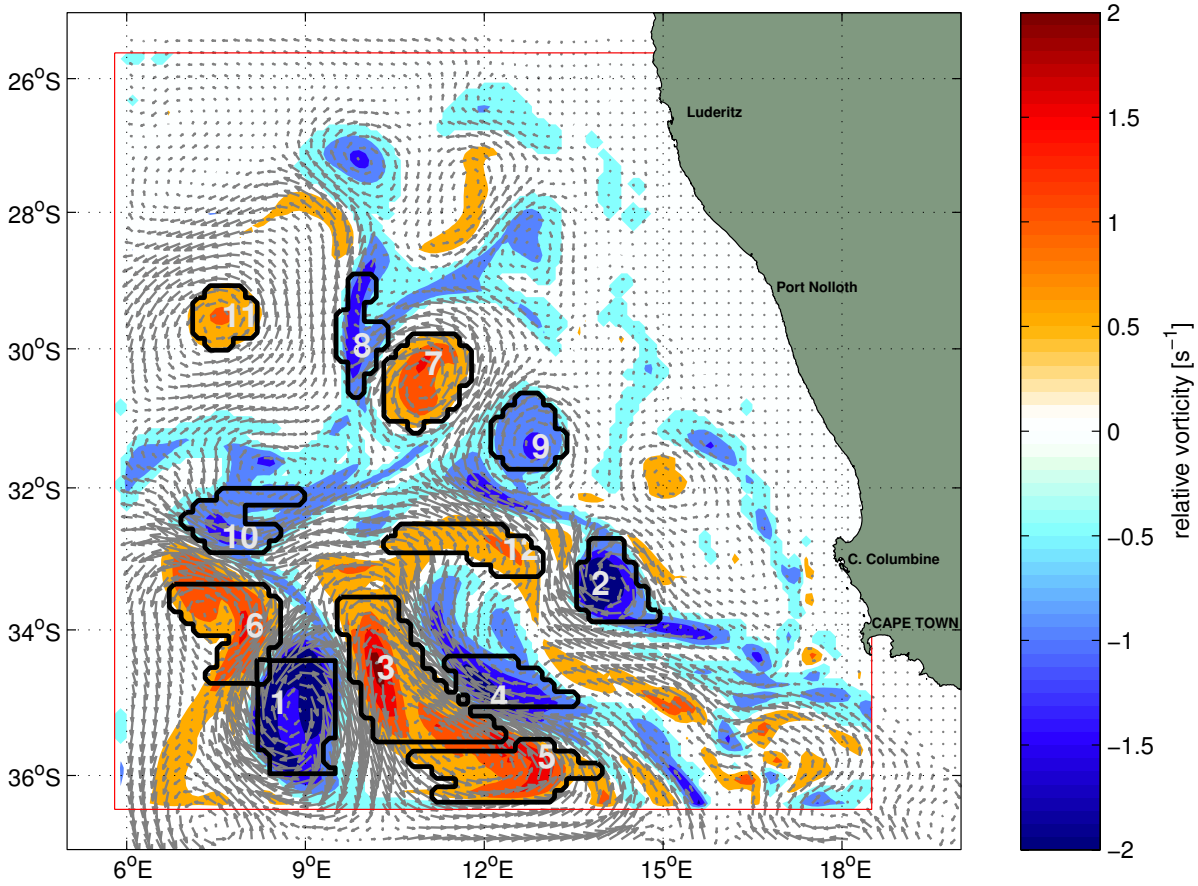

Figure 2. Wavelet analysis of the relative vorticity field (shaded colors, [s^{-1}]) at depth -200 m on day 9 / month 10 / year 7. 12 patterns are identified (black contours) and numbered in white at the position corresponding to the eddy center. The velocity field is shown with arrows. The red square shows the 128×128 gridpoint domain of the wavelet analysis.

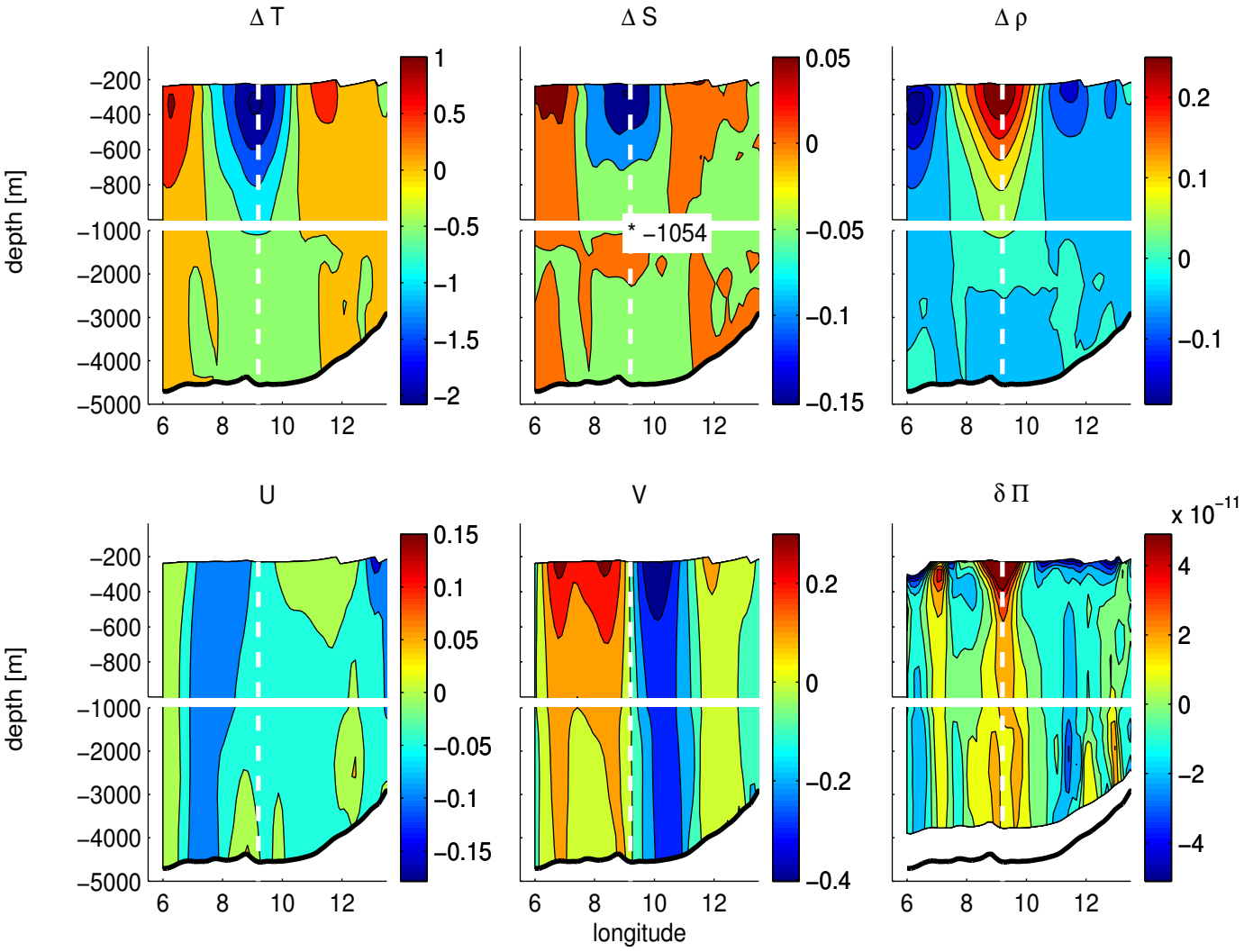

Figure 3. Vertical zonal sections of temperature anomaly [^{o}C], salinity anomaly [psu], potential density anomaly [kg m^{-3}], meridional velocity component [m s^{-1}], zonal velocity component [m s^{-1}], potential vorticity anomaly [m^{-1} s^{-1}] (from left to right and from top to bottom) for cyclone Asterix on day 6 / month 1 / year 8. The eddy center is indicated with a dotted line and its lower limit is given in the upper middle panel. The vertical axis is stretched to show in more details the upper fraction of the eddy.

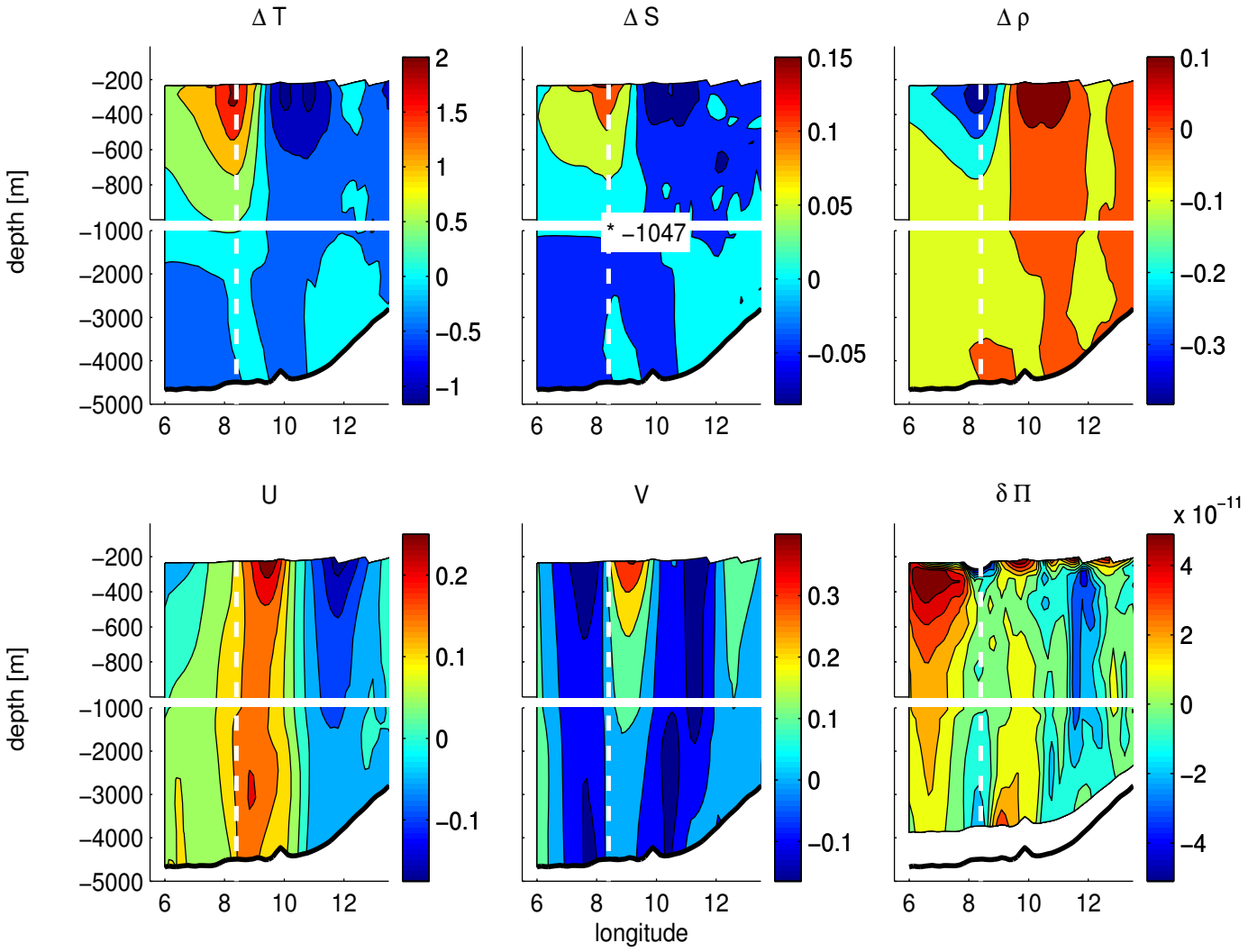

Figure 4. Same as Fig. 3 but for anticyclone Panoramix on day 1 / month 9 / year 7.

a)

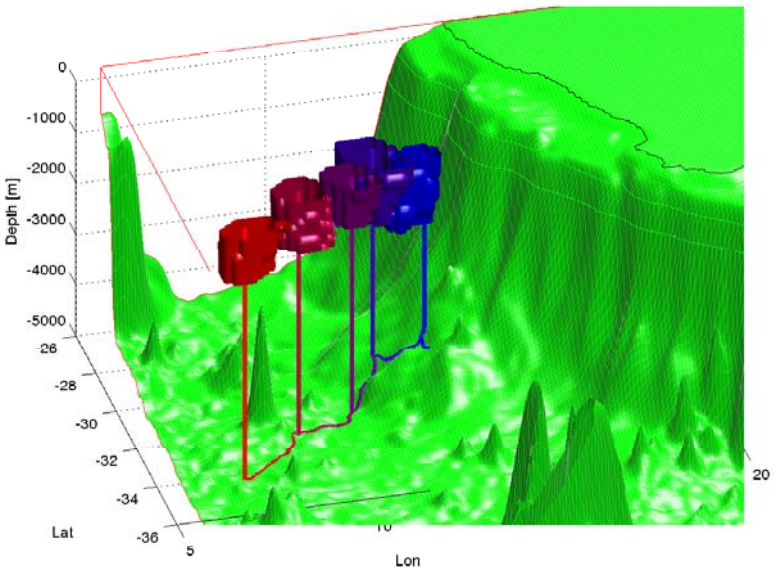

b)

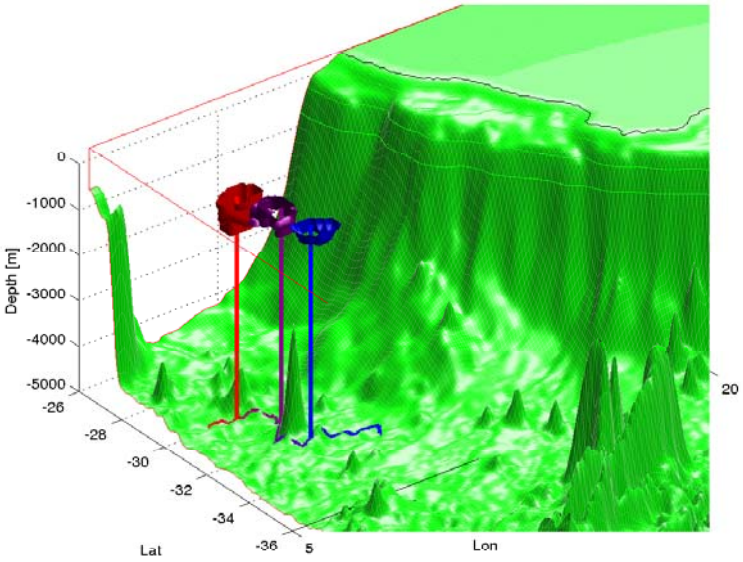

Figure 5. a) Asterix and b) Panoramix displacements. Color denotes time, from blue (freshly-formed eddy) to red (ageing eddy).

a)

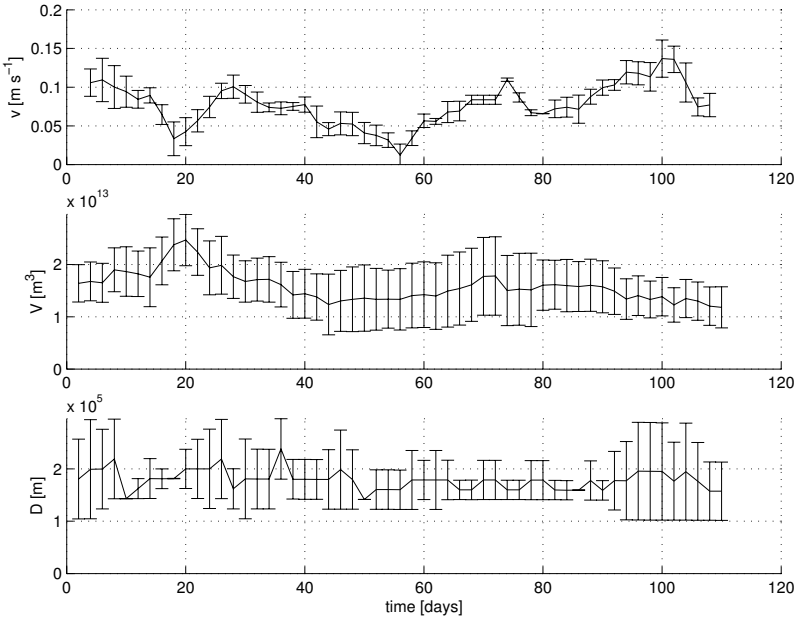

b)

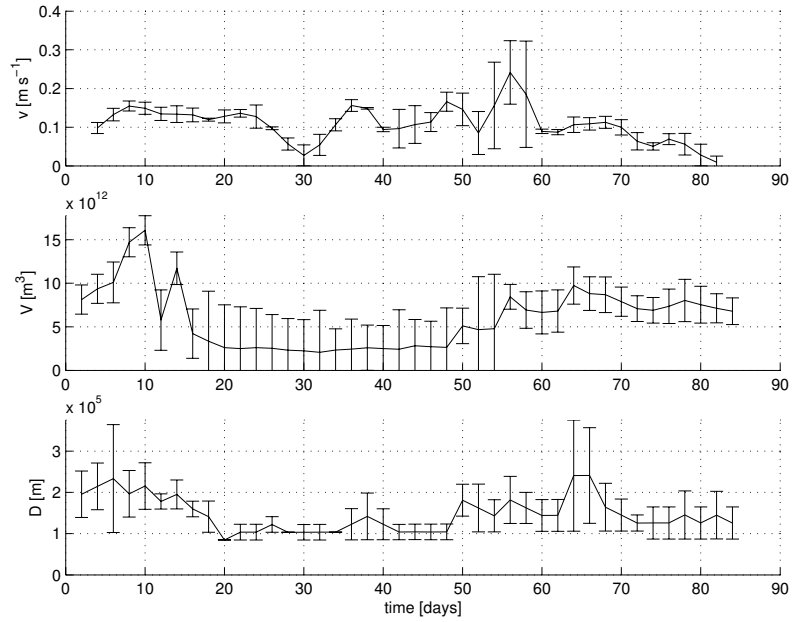

Figure 6. Time series of eddy velocity [m s^{-1}], volume [m^3] and diameter [m] (from top to bottom). Eddy ages [days] are given in abscissa. a) Asterix, b) Panoramix.

a)

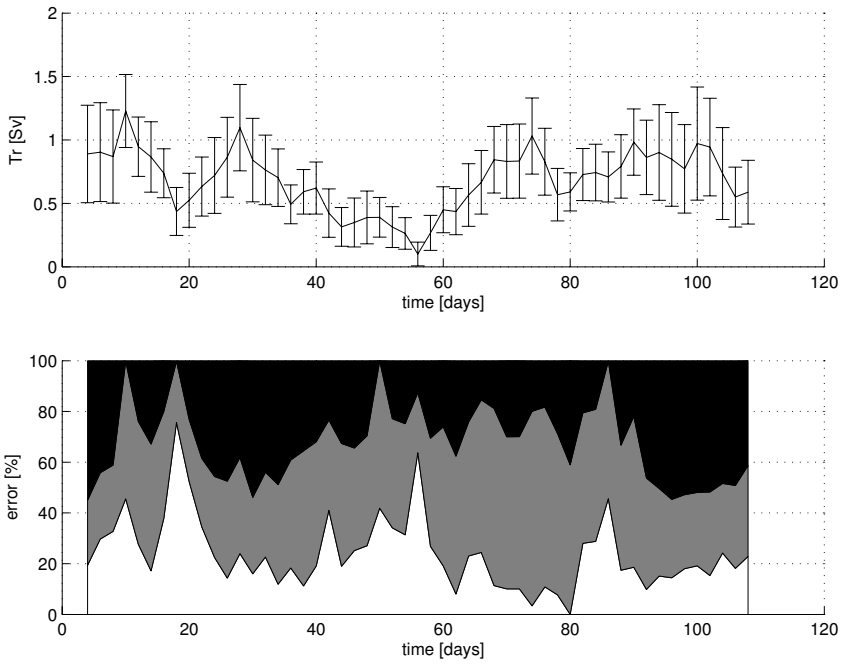

b)

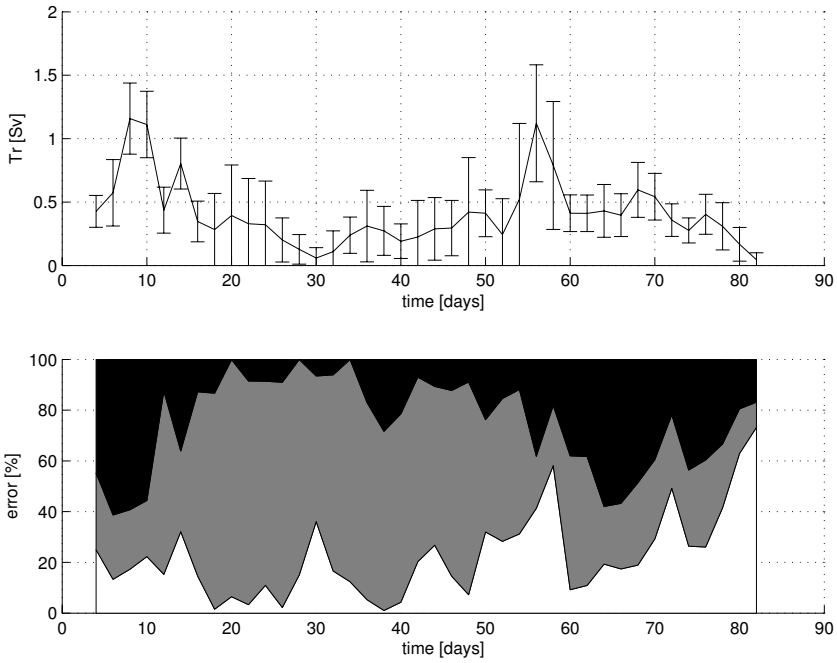

Figure 7. Time series of transport with associated uncertainty [Sv] and corresponding sources of error (v_{err} white, V_{err} gray, D_{err} black) [%]. Eddy ages [days] are given in abscissa. a) Asterix, b) Panoramix.

a)

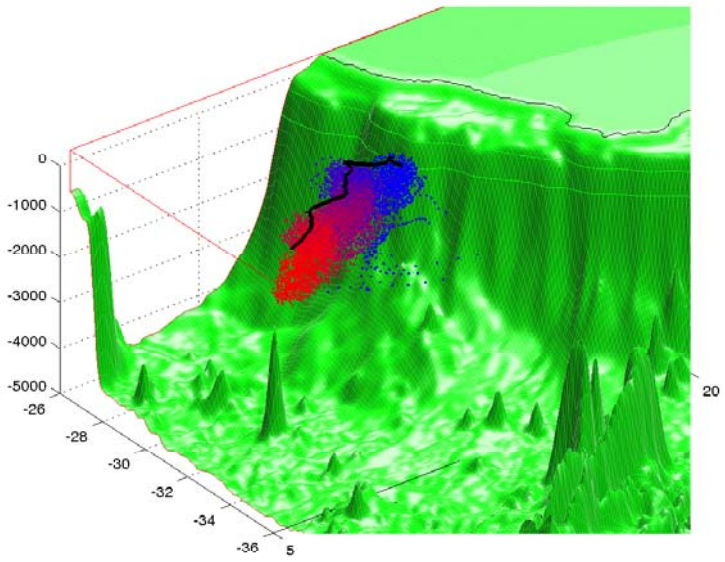

b)

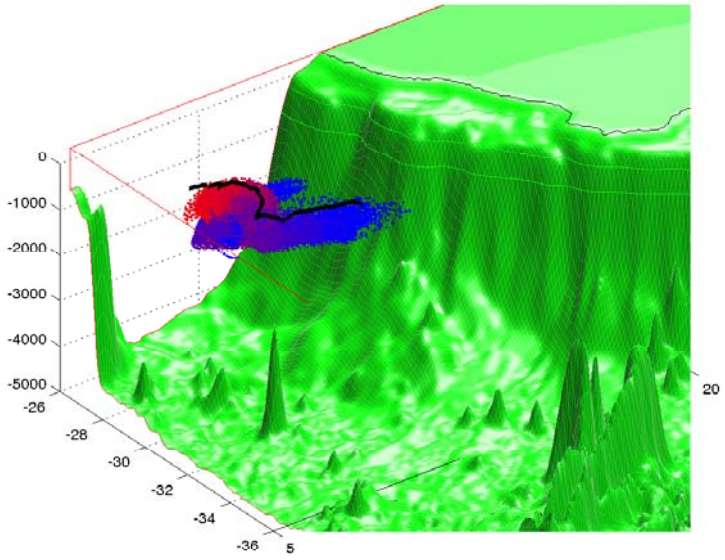

Figure 8. Backward 3D trajectories for particles initialized at the westernmost position calculated for each eddy. Color denotes time, from blue (freshly-formed eddy) to red (ageing eddy). Black lines represent the eddy center trajectories at -200 m as diagnosed with the wavelet analysis. a) Asterix, b) Panoramix.

a)

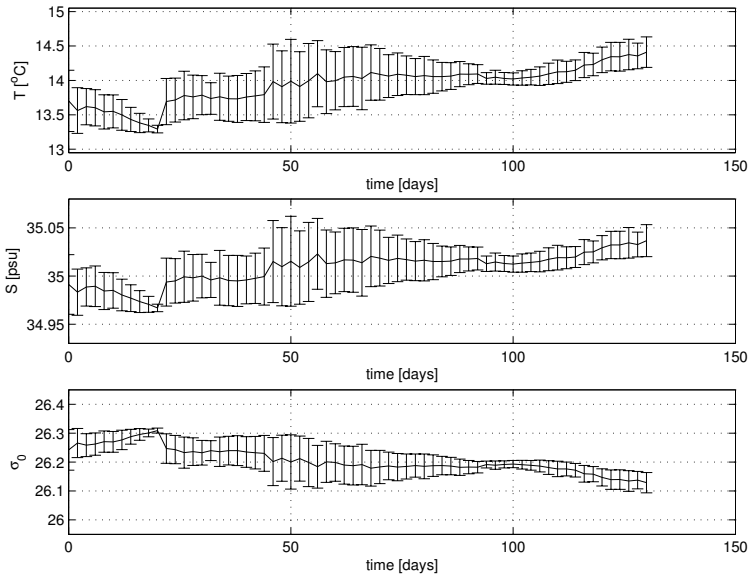

b)

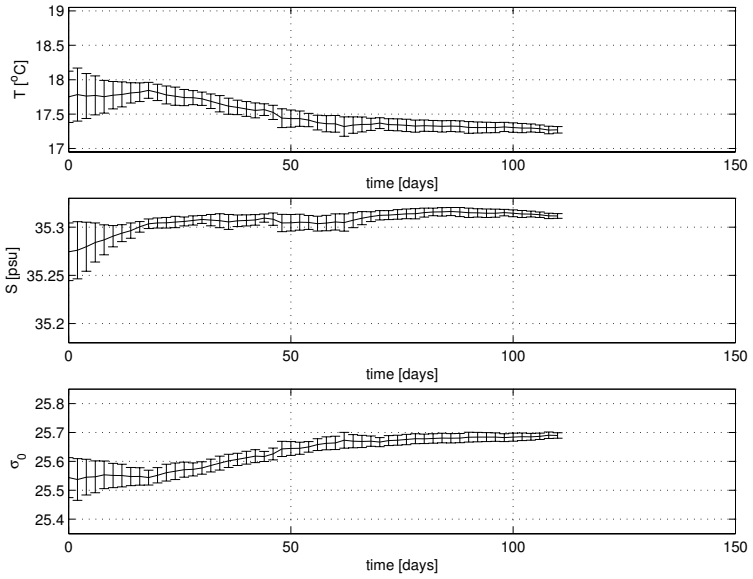

Figure 9. Time series and related standard deviations for average temperature [^{o}C], salinity [psu] and potential density [sigma zero units] calculated from model data at depth -200 m over each eddy area. Eddy ages [days] are given in abscissa. a) Asterix. b) Panoramix.

a)

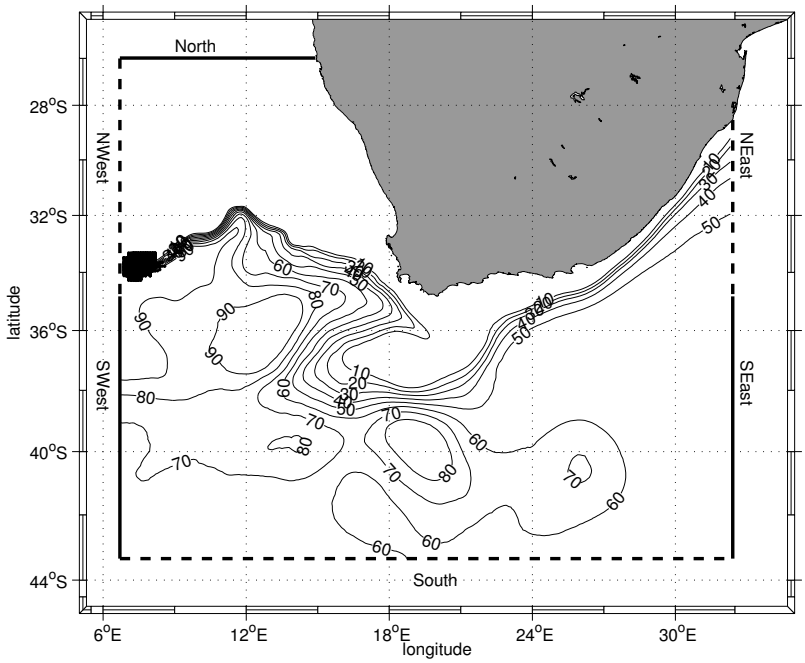

b)

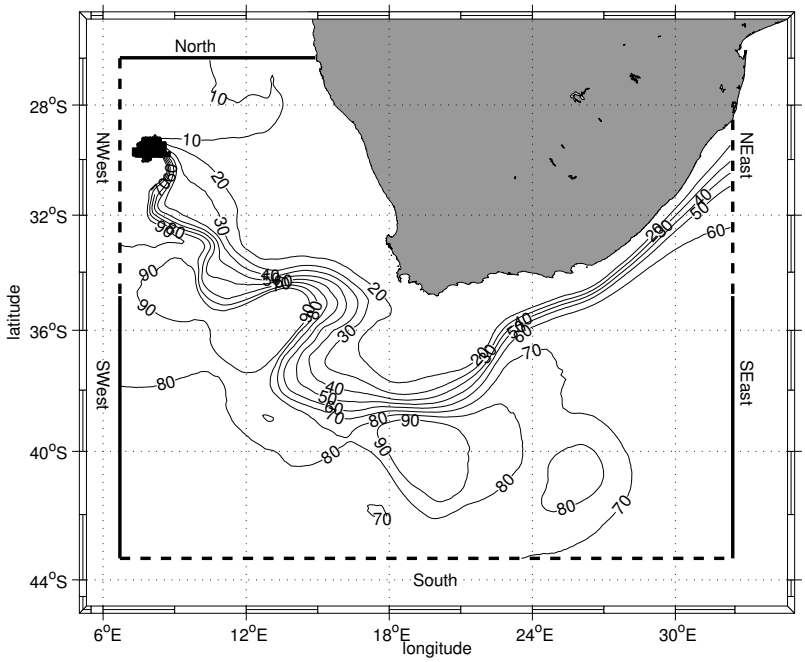

Figure 10. Integrated diagnostic of particle displacements with a 10% contour interval related to the total number of particles used to describe each eddy (see text for details). a) Asterix (experiment A33), b) Panoramix (experiment P46).

a)

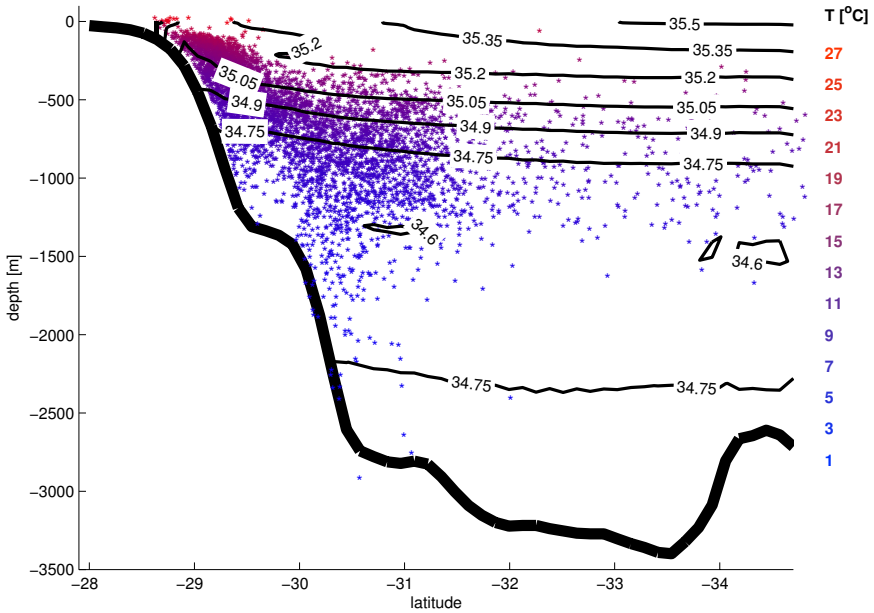

b)

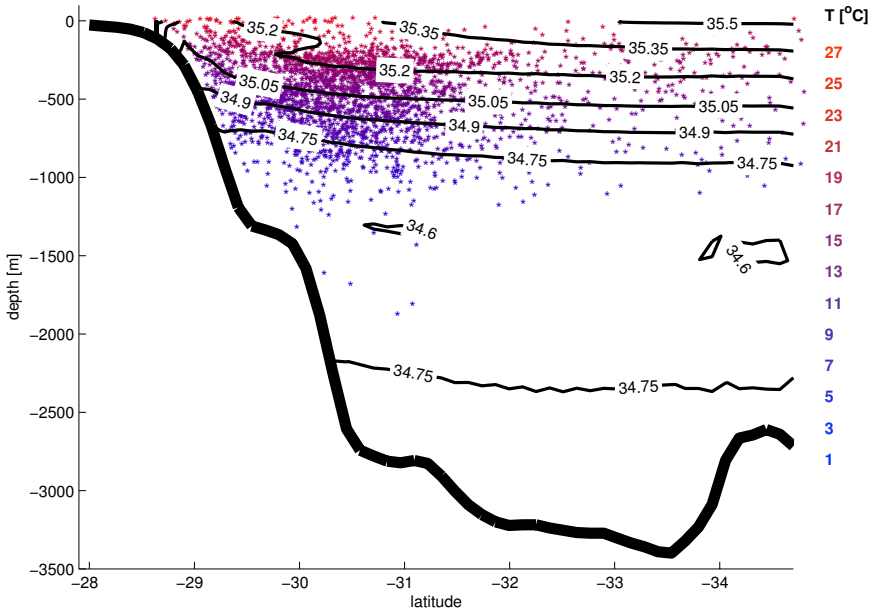

Figure 11. Space distribution (dots) and temperature (color scale) for particles originating in the Agulhas Current at longitude 32.4^{o}E. Annual mean salinity [psu] is contoured. a) Asterix (experiment A33), b) Panoramix (experiment P46).